

THE SOUTHERN GALACTIC PLANE SURVEY: THE TEST REGION

N. M. MCCLURE-GRIFFITHS,¹ A. J. GREEN,² JOHN M. DICKEY,¹ B. M. GAENSLER,^{3,5} R. F. HAYNES,⁴ & M. H. WIERINGA⁴*Accepted by the Astrophysical Journal*

ABSTRACT

The Southern Galactic Plane Survey (SGPS) is a project to image the H I line emission and 1.4 GHz continuum in the fourth quadrant of the Milky Way at high resolution using the Australia Telescope Compact Array (ATCA) and the Parkes Radio Telescope. In this paper we describe the survey details and goals, present $\lambda 21$ -cm continuum data, and discuss H I absorption and emission characteristics of the SGPS Test Region ($325.5 \leq l \leq 333.5$; $-0.5 \leq b \leq +3.5$). We explore the effects of massive stars on the interstellar medium (ISM) through a study of H I shells and the H I environments of H II regions and supernova remnants. We find an H I shell surrounding the H II region RCW 94 which indicates that the region is embedded in a molecular cloud. We give lower limits for the kinematic distances to SNRs G327.4+0.4 and G330.2+1.0 of 4.3 kpc and 4.9 kpc, respectively. We find evidence of interaction with the surrounding H I for both of these remnants. We also present images of a possible new SNR G328.6-0.0. Additionally, we have discovered two small H I shells with no counterparts in continuum emission.

Subject headings: ISM: structure — supernova remnants: individual: (G327.4+0.4, G330.2+1.0) — H II regions: individual: (RCW 94) — radio lines: ISM — radio continuum: ISM

1. INTRODUCTION

Surveys of the Milky Way allow us to look at the energetics and structure of our own Galaxy with spatial resolution that is unattainable in other galaxies. The inner Galaxy, in particular, provides a number of scientific opportunities. In the 1960's and 70's Galactic neutral hydrogen (H I) and continuum were mapped using single dish radio telescopes with low spatial resolution (eg. Weaver & Williams 1974; Goss & Shaver 1970). As a result, much of what we know about the structure of the Galactic H I is restricted to large scales. In other wave-bands Galactic surveys are much more up-to-date. In the infrared, X-ray, and H α the inner Galaxy has been mapped extensively, while H I remains seriously under-sampled. Over the past five years the H I atlas of the Galaxy has been greatly improved by the Dominion Radio Astrophysical Observatory's (DRAO) Canadian Galactic Plane Survey (CGPS) which covers a longitude range of $l = 74^\circ$ to 147° using a combination of interferometer and single dish data to image the Galaxy at a resolution of one arcminute (Taylor 1999). Despite the contributions of the CGPS to our knowledge of Galactic H I, the inner Galaxy remains neglected.

We have recently begun the Southern Galactic Plane Survey (SGPS), a large-scale project to image the $\lambda 21$ -cm continuum and H I spectral line in the fourth quadrant of the Galactic Plane with high angular and velocity resolution (Dickey et al. 1999; McClure-Griffiths et al. 1999). The SGPS makes use of high spatial resolu-

tion data from the Australia Telescope Compact Array (ATCA) and short spacing information from the Parkes 64m single dish.⁶ The final project will provide a complete H I dataset of $253^\circ \leq l \leq 358^\circ$ and $-1.0 \leq b \leq +1.0$ at an angular resolution of $2'$, and with velocity resolution of $\Delta v = 0.82 \text{ km s}^{-1}$. In addition, we have extended the single dish coverage to $b = \pm 10^\circ$ in order to study large scale structures which protrude from the Galactic plane.

This dataset is particularly useful for studying the structure and dynamics of the neutral medium, on which massive stars have a significant impact. O and B stars not only affect the medium through ionization, as in the case of H II regions, they also perturb the medium through winds and at the end of their lives, as supernovae. The resultant supernova remnants (SNRs) plow shocks through the neutral medium, ionizing and compressing the medium and leaving a lasting impression. Not only do H II regions and SNRs impact the ISM, the structure of the ISM - particularly density enhancements - affects the morphology of H II regions and SNRs. After the SNR or H II region has ceased to exist in continuum, the imprint may remain in the ISM in the form of an H I shell. Because of the large range of spatial scales sampled with the combined Parkes and ATCA data, the SGPS is an ideal dataset in which to explore these effects.

In this paper we introduce the details of the Southern Galactic Plane Survey with attention to H I spectral line and $\lambda 21$ -cm continuum data from the SGPS Test Region ($325.5 \leq l \leq 333.5$; $-0.5 \leq b \leq +3.5$). Other scien-

¹ Department of Astronomy, University of Minnesota, 116 Church Street SE, Minneapolis, MN 55455; naomi@astro.umn.edu, john@astro.umn.edu

² Astrophysics Department, School of Physics, Sydney University, NSW 2006, Australia; agreeen@physics.usyd.edu.au

³ Center for Space Research, Massachusetts Institute of Technology, 70 Vassar Street, Cambridge, MA 02139; bmg@space.mit.edu

⁴ Australia Telescope National Facility, CSIRO, P.O. Box 76, Epping, NSW 2121, Australia; rhaynes@atnf.csiro.au, mwiering@atnf.csiro.au

⁵ Hubble Fellow

⁶ The Parkes telescope and the ATCA are part of the Australia Telescope, which is funded by the Commonwealth of Australia for operation as a national facility managed by the Commonwealth Scientific and Industrial Research Organisation.

tific highlights from the SGPS are discussed elsewhere: two large H I shells discovered in the Parkes data are presented in McClure-Griffiths et al. (2000b), preliminary images of H I emission and absorption features are presented in McClure-Griffiths et al. (2000a), and the polarization properties of the Test Region are presented in Gaensler et al. (2000a). Here we explore the connections between the H I and λ 21-cm continuum images of the Test Region. In §1.1 & 2 we describe the survey objectives, observing and data analysis strategies. In §3 we discuss the λ 21-cm continuum emission. H I absorption towards continuum sources is discussed in §4. We have chosen a representative sample of H II regions and supernova remnants (SNRs) to study the relationship between the continuum emission from these objects and the surrounding H I environments in §5. The Test Region is an excellent area to initiate such a study as it contains many H II regions and SNRs, as well as extended emission structure. Using H I absorption and H I morphological matches to the continuum emission, we seek to create a three-dimensional view of the Galaxy in this subregion.

1.1. Survey Objectives

The general goal of the Southern Galactic Plane Survey is to provide a dataset with which to study the structure and dynamics of the neutral hydrogen (H I) in the inner Galaxy. Previous studies of the inner Galaxy have lacked the sensitivity and resolution necessary to study the physical processes of the interstellar medium (ISM) over a large range of spatial scales. Though the specific goals of the SGPS are numerous, we will highlight a few below:

- The SGPS will allow us to address questions about the spatial distributions and scale heights of the warm and cool components of the neutral medium in order to understand the thermal phases of the interstellar medium.
- Combining the Parkes and ATCA data, we will be able to probe the interstellar medium through a broad range of spatial scales in order to develop a statistical interpretation of the neutral ISM throughout the inner Galaxy.
- H I emission data over the large range of spatial scales available in the SGPS will allow us to detect a full sample of H I shells with which to study not only the formation of shells - particularly of the largest, most enigmatic ones - but also their distribution in the Galaxy and global effect on Galactic structure.
- A number of H I self-absorption (HISA) features are apparent in the SGPS Test Region (McClure-Griffiths et al. 2000a). HISA, where cold H I clouds absorb the diffuse background H I emission, is an excellent probe of the distribution of the coldest, most compact H I clouds. Further exploration of these features will be presented in a subsequent paper (Dickey et al. 2000).
- The dataset will provide H I absorption spectra for distance estimates of many Galactic objects and may be useful in identifying those extragalactic sources located close to the Galactic plane.

- The inclusion of full polarization information for the continuum data will allow us to explore the polarization structure of individual objects, such as supernova remnants, and to investigate the Galactic magnetic field structure using the polarization of the diffuse background emission. Results of the polarization properties of the Test Region appear in Gaensler et al. (2000a).

2. OBSERVATIONS AND ANALYSIS

Observations of the SGPS Test Region were made with the Australia Telescope Compact Array (ATCA; Frater, Brooks, & Whiteoak 1992) and Parkes Radio Telescope. The ATCA is an east-west synthesis instrument near Narrabri NSW, with six 22 m antennas on a 6 km track. Five antennas are movable into configurations with baselines between 31 m and 6 km. The ATCA data consist of a 190 pointing mosaic covering $325^{\circ}.5 \leq l \leq 333^{\circ}.5$ and $-0^{\circ}.5 \leq b \leq +3^{\circ}.5$. These data were obtained during five separate observing sessions between April 1997 and April 1998. The observing dates and times are given in Table 1. The observations were made with several compact array configurations - 750A, 750C, 750D, and 375 - in order to obtain maximum sensitivity to large scale structures. Each of the 190 pointings was observed in forty 30 s snapshots at a broad range of hour angles for good u - v coverage. The pointings for the Test Region were arranged on a square grid with 15' separation (Nyquist) as determined by the ATCA primary beam FWHM, which is 33' at λ -21 cm. The pointing centers are plotted on the 21-cm continuum ATCA image of the SGPS Test Region shown in Fig. 1. The ATCA feeds receive two orthogonal linear polarizations, X and Y . All observations were recorded in a wideband continuum mode with 32 channels, each 4 MHz, across a 128 MHz total bandwidth with polarization products XX , YY , XY , and YX to enable calculation of all four Stokes parameters; and simultaneously in a spectral line mode with polarization products XX and YY in 1024 channels across a 4 MHz total bandwidth. The continuum data are centered on $\nu = 1384$ MHz, whereas the spectral line data are centered on $\nu = 1420.0$ MHz and have channel separation of $\Delta\nu = 0.82$ km s $^{-1}$ (3.9 kHz).

Data editing, calibration, and imaging of the ATCA data are carried out in the MIRIAD data reduction package (Sault & Killeen 2000). The source PKS B1934-638 is used for flux density and bandpass calibration and was observed once per observing session. A flux density of 14.94 Jy at 1420 MHz is assumed (Reynolds 1994). PKS B1934-638 has no detectable linear polarization and can therefore be used to solve for the polarization leakages. Polarization leakages are also calculated for the sources MRC B1613-586 and MRC B1431-48 which were observed approximately once every hour for calibration of the time-variation in complex antenna gains.

The individual pointings were linearly combined and imaged using a standard grid-and-FFT scheme with super-uniform weighting. Like uniform weighting, super-uniform weighting minimizes sidelobe levels to improve the dynamic range and sensitivity to extended structure. Uniform weighting reduces to natural weighting, however, if the field of view is much larger than the primary beam,

as is the case for large mosaics. Super-uniform weighting overcomes this limitation by decoupling the weighting from the field size (Sault & Killeen 2000). In this manner super-uniform weighting attempts to minimize sidelobe contributions from strong sources over a region smaller than the full field being imaged and therefore is typically more successful than uniform weighting on large mosaics (Sault et al. 1996).

The specifics of the calibration and imaging of ATCA polarization data are described in (Gaensler et al. 2000a), here we discuss only the Stokes I continuum and H I data. Two H I data cubes were produced. In one cube the continuum emission was subtracted from the H I $u-v$ data using the MIRIAD task `uvlin`. The second cube, for use in absorption studies, contains continuum emission. The resultant synthesized beam for both cubes and the continuum image is $124''.9 \times 107''.5$ ($\alpha \times \delta$). For the data presented here the 6 km baselines of the ATCA were not used. However, the long baselines are retained for some absorption studies, such as those presented in Dickey et al. (2000). Joint deconvolution was performed on the full linear mosaics using a maximum entropy algorithm implemented in MIRIAD task `mosmem` (Sault et al. 1996). The method of joint deconvolution is very effective for maximizing the $u-v$ coverage attainable in mosaiced observations (Sault et al. 1996). Despite deconvolution, some sidelobes are visible around strong point sources in the continuum and H I images.

Though mosaicing allows us to recover angular scales larger than normal interferometric observations by reducing the effective shortest projected baseline, we are nonetheless limited in practice to angular scales smaller than $\theta = \lambda/(d - D/2)$, where $d = 30.6$ m is the shortest baseline of the ATCA, and $D = 22$ m is the diameter of a single antenna. This limits the ATCA data to angular scales smaller than $\theta \approx 36'$. In order to recover information on larger size scales, the ATCA mosaic must be combined with single dish data from the Parkes Radio Telescope.

The Parkes Radio Telescope is a 64 m antenna situated near Parkes NSW, Australia. It has a thirteen beam, $\lambda 21$ -cm receiver package at prime focus (Staveley-Smith et al. 1996). The SGPS Test Region was observed on 1998 December 15-16. The Parkes survey was subsequently expanded to $b = \pm 10^\circ$ for more complete coverage of large scale structures during additional observing sessions: 1998 June 18-21, 1999 September 18-27, and 2000 March 10-15. Observations were made by the process of mapping ‘‘on-the-fly’’ with the inner seven beams of the multibeam system. Data were recorded in 5 s samples, while scanning through three degrees in Galactic latitude. The data were taken in frequency switching mode using the narrowband back-end (Haynes et al. 1998), with a total bandwidth of 8 MHz across 2048 channels. Though the Parkes data are frequency switched, total power information for each sample is retained. Each sample was divided by the previous frequency switched sample and the residual bandpass shape fitted with a series of Fourier components. The spectra were then multiplied by the mean of the reference signal over the spectrum to reconstruct the continuum emission with a flat baseline. Absolute brightness temperature calibration of the H I line data was performed from obser-

vations of the IAU standard regions S6 and S9 (Williams 1973). A detailed description of the observing strategy, calibration, and imaging procedures is found in McClure-Griffiths et al. (2000b). Off-line channels were used for continuum subtraction and to produce the continuum image using the AIPS task `IMLIN`. The Parkes data on the SGPS Test Region have an angular resolution of $\sim 15'$. The final, calibrated data have a bandwidth of 4 MHz with 1024 channels, such that the velocity resolution of 0.82 km s^{-1} matches the ATCA data.

It should be noted that the data presented here have not been corrected for the effects of stray radiation. Stray radiation leakage from bright H I emission through the back sidelobes of a single dish beam introduces baseline errors which are typically between 0.5 K and 2 K (Kalberla, Mebold & Reich 1980). When compared to low latitude Galactic spectra, this is a small percentage, but it does nonetheless limit the sensitivity and accurate representation of extended features in the Parkes data. The data for the entire survey will have a first order stray radiation correction applied. A complete correction requires a low resolution survey of the entire sky with a known antenna pattern in order to reconstruct the stray radiation at every point on the sky, at any azimuth and elevation, and at any time of the year. Such a task is beyond the scope of this project. A first order correction, however, can be done by re-observing the survey region at different times of the year and comparing the spectra. The velocity shifts caused by the Earth’s motion around the Sun result in excess emission at different velocities. We have, therefore, re-observed the full survey region four times at three month intervals around the year and we will compare each spectrum. The minimum value at each velocity will be a reasonable upper limit to the stray radiation corrected profile, good to within ~ 0.5 K of T_B .

The final step of imaging involves combining the Parkes and ATCA data. The data may be combined in the Fourier domain after deconvolution of the individual images or in the $u-v$ plane prior to deconvolution. Stanimirović (1999) showed that the results are comparable using either method, but that combining after deconvolution produced results that were typically more consistent than with other methods. Comparison of our data combined in both ways shows similar results. We have chosen, therefore, to combine the data in the Fourier domain after deconvolution. In this method, the interferometric data H I and continuum data are imaged and deconvolved, the single-dish data are imaged and the clean interferometric and single-dish images are Fourier transformed and combined. This technique is implemented in the MIRIAD task `immerge`. Slight differences in calibration can lead to the necessity of a relative calibration factor by which the single-dish dataset is multiplied before combination. This calibration factor is determined by comparing the datasets in the Fourier plane at every pixel and frequency in the range of overlapping spatial frequencies. In order to calculate the calibration factor both images must be deconvolved, a step which requires a good knowledge of the single-dish beam (Stanimirović 1999). Using a two dimensional Gaussian with FWHM $15''.5$ for the Parkes beam and by comparing the Parkes and ATCA continuum images of a strong, compact source in the Test Region, we calculated a relative

calibration factor of 1.19. Two combined H I data cubes were created, one containing the continuum emission for absorption studies and one which had the continuum subtracted for emission studies. The continuum images were combined in the same way as the cube and with the same calibration factor. The combined Parkes and ATCA 21-cm continuum image is shown in Fig. 3.

The combined data are sensitive to all angular scales from the synthesized beam size, $124''.9 \times 107''.5$ ($\alpha \times \delta$), up to the image size, $8^\circ \times 4^\circ$ ($l \times b$) for the Test Region. Because of the fine scale structure seen in the velocity domain, no Hanning smoothing was applied to the data. Each channel image has a velocity separation of 0.82 km s^{-1} . Channel images from the continuum subtracted combined data cube are shown in Fig. 2. Every fourth channel from $v = -127 \text{ km s}^{-1}$ to $v = 79 \text{ km s}^{-1}$ is shown. The rms noise in the channel images is $\sim 2.4 \text{ K}$ of T_B for the ATCA data, $\sim 100 \text{ mK}$ of T_B for the Parkes data and $\sim 2.3 \text{ K}$ of T_B for the combined dataset. The rms noise in the continuum images is $\sim 5.5 \text{ mJy beam}^{-1}$ for the ATCA data, $\sim 500 \text{ mJy beam}^{-1}$ for the Parkes data (beam size $15''.5 \times 15''.5$), and $\sim 7 \text{ mJy beam}^{-1}$ for the combined data.

3. CONTINUUM EMISSION

The combined $\lambda 21$ -cm continuum image of the SGPS Test Region is shown in Fig. 3. Most sources have been previously catalogued as H II regions or SNRs (Avedisova 1997; Caswell & Haynes 1987; Green 2000; Whiteoak & Green 1996). There are also many unresolved sources scattered throughout the Test Region. H I absorption measurements towards many of these suggest that most are extragalactic. This region has been studied in H α by Georgelin et al. (1994) as part of an extensive H α survey of the Southern Galactic Plane. As shown in the Fig. 4, a diagram of the expected velocities and spiral arms in the fourth quadrant, the Test Region line of sight crosses both the Sagittarius-Carina and Scutum-Crux spiral arms and runs tangent to the Norma arm at $l \approx 327^\circ$. As a result this region has a particularly high density of continuum sources.

3.1. Discrete Sources

We describe here the more prominent discrete sources in the SGPS Test Region. These sources are marked in on the MOST 843 MHz continuum image shown in Fig. 5. Several individual sources are discussed in detail below with comment given about their associated H I emission. Starting at the lower longitude end, the first strong source is RCW 94 (Rodgers, Campbell, & Whiteoak 1960; Shaver, McGee, & Pottasch 1979) at $l = 326^\circ 3$, $b = +0^\circ 8$, with an angular diameter of about $18'$. This ring-like structure is an H II region, with strongest emission to the lower left. There is a smaller region adjoining the H II region at $l = 326^\circ 4$, $b = +0^\circ 9$. At $l = 326^\circ 7$, $b = +0^\circ 8$ is another H II region, RCW 95. Directly below RCW 95 is the brighter, extended H II region G326.65+0.59 (Georgelin et al. 1994). Closer to the Plane at higher longitudes is a very extended thermal filamentary structure G326.96+0.03. This source has arcs of emission above and below a centralized bright knot. Because these sources are all at the same distance, we refer to the grouping of RCW 94, RCW 95, G326.65+0.59, and

G326.96+0.03 as the RCW 94-95 H II region complex.

Above the high longitude edge of the G326.96+0.03 arc is SNR G327.4+0.4, a large shell type SNR with enhanced limb brightening to the lower left. Further from the Plane than G327.4+0.4 there is a smaller, weaker supernova remnant, SNR G327.4+1.0. This source has a nearly closed arc extending to higher latitudes. At slightly higher longitudes there is a region of extended emission comprised of several thermal sources grouped at G327.83+0.11. At higher longitudes and lower latitudes than these sources there is another H II region, G327.99-0.09. Near $l = 328^\circ$ is the compact H II region G328.31+0.45 and the extremely bright Crab-like SNR G328.4+0.2 (Gaensler et al. 2000b).

At higher longitudes, the compact source G328.81-0.08 is classified as an H II region in Caswell & Haynes (1987, hereafter CH87) on the basis of a recombination line detection. However, examination of the Midcourse Space Experiment (MSX; Egan et al. 1998) band A ($6.8 - 10.8 \mu\text{m}$) image shows only a small infrared source, IRAS 15550-5306, slightly offset from the center of G328.81-0.08. This infrared source has a FWHM of $\sim 30''$, whereas the offset $\lambda 21$ -cm source has a FWHM of $\sim 3'$. It is unclear whether the infrared source is the same as the radio source.

About $30'$ from G328.81-0.08 there is an extended source centered at $l = 328^\circ 6$, $b = 0^\circ$. Fig. 6 shows the combined Parkes and ATCA 1.4 GHz SGPS continuum image of this region and the MOST 843 MHz image of the same area. In the SGPS image the source has a mostly filled, double loop morphology of angular diameter $\sim 0^\circ 5$, and internal filamentary structure. Only the edges of the source are observed as filaments at the $\sim 15 \text{ mJy beam}^{-1}$ level in the MOST image. The smooth, extended emission observed in the SGPS image is not detected by MOST. There is no counterpart to this emission in the MSX band A image. The fact that no corresponding IR emission is detected from this source suggests that the emission is non-thermal and we propose that it is a new SNR candidate, G328.6-0.0. There are also several long overlapping thermal filaments visible in both of the radio continuum images and the MSX image. These thermal filaments do not appear to be directly associated with this double loop SNR candidate, G328.6-0.0, but extend to $b = 0^\circ 5$. Embedded within the left edge of the SNR candidate is an unresolved source at $l = 328^\circ 59$, $b = -0^\circ 11$ which does not appear in the MSX image, suggesting that it too is either non-thermal or extragalactic.

Near $l = 329^\circ$ there are two H II regions, G329.35+0.14 and G329.49+0.21. At larger longitudes there is the large supernova remnant, SNR G329.7+0.4, which accounts for much of the extended emission in this portion of the Test Region. The large ($\Delta\theta \sim 40'$) remnant consists of many loops. Above G329.7+0.4 is a large ($\sim 20'$) loop of thermal emission which is also visible in the MSX images. This may be an extended H II envelope (EHE) as similarly suggested for the area around $l = 312^\circ$ (Whiteoak, Cram, & Large 1994). This region appears connected to large arcs of thermal emission extending above and below SNR G330.2+1.0. SNR G330.2+1.0 is a composite remnant with irregular emission that does not seem to form a clear shell. Between $l = 330^\circ 2$ and $l = 330^\circ 9$ there are few bright discrete sources. The area is largely filled with extended emission.

Another large H II complex is located around $l = 331^\circ$, including the H II regions: G331.03-0.15, G331.26-0.19, G331.52-0.07; and at the high longitude limit of the Test Region: SNR G332.0+0.2. SNR G332.0+0.2 is a mostly complete shell of angular diameter $\sim 10'$. Further above the Plane are two large H II regions: G331.35+1.07 and G331.36+0.51.

3.2. Extended Continuum Emission

Throughout the Test Region there is diffuse emission which decreases in intensity with increasing latitude. Fig. 7 shows three slices across the Test Region continuum image, all at $l = 328^\circ.7$. The first slice is across the ATCA image alone, the second across the Parkes image alone, and the third is across the combined image. It is clear that the ATCA data is not sensitive to the large scale Galactic emission, but resolves the individual sources. The slice across the Parkes image shows the large-scale decrease in emission, but the low resolution does not clearly delineate the individual sources. The combined image, however, shows both the large-scale emission and the resolved sources. From this slice it is obvious that both single dish and interferometric data are necessary to understand the relationship between discrete and extended Galactic continuum emission.

Though some of the extended emission in the Test Region is smooth and can be attributed to the diffuse Galactic background, there is also structure in the emission. It is not immediately obvious whether the structure can be attributed to the Galactic background, whether it is associated with discrete continuum sources, or whether it has an altogether different nature. This question was addressed by Whiteoak, Cram, & Large (1994) who carefully examined a $3^\circ \times 2^\circ$ region in the Plane around $l = 312^\circ$ from the MOST Galactic Plane Survey (Green et al. 1999). They note low surface brightness, extended emission in the high resolution 843 MHz continuum images and suggest that this is associated with the ionized ISM. The emission they detect is thermal and they relate some of it to extended H II envelopes (EHEs) around H II regions. The MOST data are only sensitive to structures up to $30'$, so it is unclear whether there are larger-scale associations amongst some of these filamentary structures. The SGPS data are sensitive to all size scales up to about four degrees and are hence well-suited to study these features.

The MOST and SGPS surveys complement each other very well. Comparison of the MOST 843 MHz image in Fig. 5 and the SGPS ATCA continuum image in Fig. 1 shows good correlation between the two interferometric images, though the MOST images are at a slightly higher angular resolution ($43''.0 \times 51''.9, \alpha \times \delta$). In both images there are filaments, typically a few arcminutes in width and up to few degrees in length. With the inclusion of the Parkes data in Fig. 3 we can observe how these filaments relate to the larger-scale diffuse emission. It appears that there are two categories of extended emission: one where filamentary structures are part of larger-scale, filled structures and one where the filaments are self-contained structures. An example of a structure which appears filled-in with the inclusion of the Parkes data is the possible SNR G328.6-0.0, as shown in Fig. 6 and described in §3.1. In this case, the loops observed in the MOST and ATCA im-

ages are observed as part of a cohesive, filled structure in the SGPS image. Clearly, the filaments are the SNR edges which the interferometers can detect, while they cannot detect the large-scale smooth emission in the center of the remnant. By contrast, there are many loops and filaments near SNR G330.2+1.0 that appear filamentary in both the MOST and SGPS images, implying that they are not part of a larger, filled structure. These filaments are visible in the MSX images, implying that they are thermal. These structures may be sheets viewed edge-on, threads, or the edges of EHEs where the surfaces are too diffuse to be detected.

4. H I ABSORPTION

In order to create a three-dimensional view of this portion of the Galaxy we have extracted H I absorption spectra towards the brighter H II regions and SNRs. The method we use to determine the HI absorption spectrum is based on averaging the spectra toward the brightest part of the continuum ("on-source spectra"), and subtracting an interpolated average of the spectra from the region surrounding the continuum source ("off-source spectra"; Dickey et al. 1992). The on-source spectra are selected based on the continuum image by setting a high threshold, typically 80% of the continuum peak, and including in the average only spectra toward pixels whose continuum brightness is above this high threshold. These on-source spectra are averaged with weighting factor equal to the continuum brightness in each pixel, which optimizes the signal-to-noise ratio in the resulting absorption spectrum. Similarly, the off-source spectra are selected toward pixels whose continuum brightness is below a low threshold, typically 20% of the continuum peak. The off-source spectra are not simply averaged, but interpolated to give a better prediction of the emission spectrum in the direction of the continuum peak. This interpolation is based on a simple bi-linear fit (least squares fitting a linear function of two dimensions) done independently for each spectral channel. The outer boundary for which spectra are included in the off-source interpolation is typically $7'$, but for the extended supernova remnant G327.4+0.2 we extend the outer boundary to $15'$. The high and low thresholds also have to be adjusted in some cases depending on the continuum flux, down to 70% for the high threshold of the faintest sources, and in the range 10% to 30% for the low threshold depending on the angular size of the continuum distribution. This interpolation process does not change the fundamental angular resolution of the survey, i.e. it is not an extrapolation on the u - v plane. So the spectra derived for both the absorption and the expected emission still correspond to one beam area of roughly $2'$ diameter.

The absorption spectrum is then determined by subtracting the interpolated off-source spectrum from the averaged on-source spectrum. The resultant optical depth spectrum, $e^{-\tau}$, is the absorption spectrum divided by the continuum flux averaged over the pixels above the high threshold. The optical depth spectra towards RCW 94 and G326.65+0.59 are shown in Fig. 8 (bottom plot) with corresponding interpolated off-source emission spectra (upper plot). The errors in the absorption spectra are generally dominated by uncertainty in the interpolated emission, particularly at low latitudes where the emission is

not smoothly distributed on scales of a few arcminutes. To estimate the error in the absorption we compute the predictions for the off-source spectra based on the bilinear fit to the emission and take the difference between these predictions and the actual spectra in each off-source pixel. The rms average of these differences gives an error envelope on the interpolated emission in the direction of the continuum peak. Dividing by the continuum flux averaged over the on-source pixels gives the optical depth error spectrum ($\pm 1\sigma$), shown in dotted lines on Figs. 8 & 9.

For the absorption feature with most extreme velocity (most negative or most positive) we define V_L , the lower limit on the distance. Following Frail & Weisberg (1990) we define the velocity corresponding to the upper distance limit, V_U , as the first emission peak ($T_b > 35$ K) beyond V_L which does not correspond to any absorption features. Upper distance limits are estimates only, since the absence of an absorption line at the higher velocity is not conclusive evidence that the continuum source is nearer than the H I emission. A region of 21-cm emission may not show absorption because the cool gas may have a covering factor less than one (i.e. there may be gaps between absorbing clouds, filled only with warm gas which does not show detectable absorption). This is unlikely for an emission region with column density of 3×10^{20} cm $^{-2}$ or more, which is implied by a line of brightness temperature greater than 35 K. Emission lines stronger than this almost always show some absorption, so our upper limit distances should be mostly valid. We assume that the velocity errors are dominated by random cloud motions on the order of 6 km s $^{-1}$ (Dickey 1997). Velocity limits and corresponding kinematic distances are given in Table 2 for sources brighter than ~ 800 mJy beam $^{-1}$. Included in the table for comparison are the radio recombination line velocities from CH87. Some individual sources are discussed in detail later.

The absorption velocities in Table 2 clearly lie in two dominant distributions, one centered around $v = -50$ km s $^{-1}$ and another centered around $v = -90$ km s $^{-1}$. Calculated isovelocity contours from the Fich, Blitz, & Stark (1989) rotation curve are plotted in Fig. 4 on the Taylor & Cordes (1993) model of Galactic spiral arms to show the velocities covered by individual spiral arms and the range of expected velocities for any given line of sight. The Test Region line of sight is marked by the wedge. Fig. 4 shows that gas between $v = -20$ km s $^{-1}$ and $v = -30$ km s $^{-1}$ is located in the Sagittarius-Carina arm. The position of this arm in velocity space is well traced by H II regions (Georgelin & Georgelin 1976; Caswell & Haynes 1987). Gas at velocities between $v = -50$ km s $^{-1}$ and $v = -75$ km s $^{-1}$ is located within the Scutum-Crux arm. As noted in CH87 there are many features around $v = -90$ km s $^{-1}$ for which the correspondence to a spiral feature is unclear. Georgelin & Georgelin (1976) assign these H II regions to the Norma arm. At $l \approx 327^\circ$ the line of sight is nearly tangent to this arm, which accounts for the large number of sources seen there. The distribution centered at $v = -90$ km s $^{-1}$ has a large spread in velocity space, extending as far as the terminal velocity near $v = -110$ km s $^{-1}$. This large velocity spread can also be explained by the line of sight remaining in the spiral arm for a significant distance near the arm tangent. Using H II

regions and diffuse H α emission, Georgelin et al. (1994) similarly note velocity distributions at $v = -20$ km s $^{-1}$, $v = -40$ km s $^{-1}$, and $v = -65$ km s $^{-1}$. They do not, however, detect H α emission near $v = -90$ km s $^{-1}$ because it is beyond the extinction limit.

From the H I absorption we determine new kinematic distances to two supernova remnants and confirm distances to a further one SNR and nine H II regions. For SNR G328.4+0.2 our absorption spectrum looks very similar to Gaensler et al. (2000b), who also found an extreme velocity of $v = 28$ km s $^{-1}$. The H II region velocities all correspond with the velocities given in CH87. The new kinematic distances for SNR G327.4+0.4 and SNR G330.2+1.0 are given in Table 2 and are discussed in detail below.

4.1. Distance Ambiguities for Individual Sources

Many of the sources presented here have distance ambiguities. Sources in the fourth quadrant with negative velocities are found inside the solar circle where each velocity corresponds to two distances. There are several methods for distinguishing between the two distances. H α emission is often used as an indicator, as it is severely absorbed at far distances. One can also make rather uncertain estimates based on associations with nearby objects of known distance, the emission spectrum towards the object, or the more likely linear size and luminosity. For H II regions with recombination velocities, comparison of the H I absorption velocity with the recombination line velocity can resolve the ambiguity (Kuchar & Bania 1994). If the most extreme H I absorption is at or near the recombination line velocity then the cloud is at the near distance. However, if the H I absorption is seen beyond the recombination line velocity then the H II region is at the far distance.

For all of the H II regions presented here we have recombination line velocities from CH87. In all cases there is no absorption significantly beyond the recombination line velocity, implying the near distance for these regions. The Georgelin et al. (1994) H α survey of this region also resolved many of the distance ambiguities through associations with stellar distances. In particular, Georgelin et al. (1994) favor the near distance for the star forming region associated with RCW 94 and RCW 95, as discussed below.

5. H I EMISSION FEATURES

5.1. The RCW 94-95 H II Region Complex

As described in Section 3, the Test Region contains many catalogued H II regions. RCW 94, RCW 95, and G326.65+0.59 are part of a large star-forming complex in the Scutum-Crux arm. H $_2$ CO and hydrogen recombination line (H109 α & H110 α) velocities of $v = -42$ km s $^{-1}$ and $v = -45$ km s $^{-1}$ have been measured for RCW 94 and 95, respectively (CH87). We have extracted H I absorption profiles towards both RCW 94 and G326.65+0.59 (see Fig. 8) which confirm these velocities, showing deep absorption out to $v = -47$ km s $^{-1}$ and $v = -43$ km s $^{-1}$, respectively. The most extreme absorption line for G326.65+0.59, centered at -46 km s $^{-1}$ is slightly broader ($\Delta v \approx 15$ km s $^{-1}$) than that for RCW 94 ($\Delta v \approx 9$ km s $^{-1}$), suggesting a more turbulent region (Shaver, McGee, & Pottasch 1979). Georgelin et al.

(1994) also note the differing line widths of these two regions. We adopt the IAU standard values for the Sun's orbital velocity, $\Theta_o = 220 \text{ km s}^{-1}$, Galactic center distance, $R_o = 8.5 \text{ kpc}$, and use the rotation curve of Fich, Blitz, & Stark (1989) to calculate distances. Assuming a common velocity of $v = -45 \pm 6 \text{ km s}^{-1}$, we find distances of $3.1 \pm 0.3 \text{ kpc}$ or $11.1 \pm 0.3 \text{ kpc}$. Georgelin et al. (1994) identify two populations of H II regions within the Scutum-Crux arm, one at $v = -40 \text{ km s}^{-1}$ and another at $v = -50 \text{ km s}^{-1}$. While they associate the RCW 94-95 complex with the $v = -40 \text{ km s}^{-1}$ population, our absorption velocities indicate absorption out to nearly $v = -50 \text{ km s}^{-1}$.

In order to resolve the distance ambiguity Georgelin et al. (1994) have identified stars of spectral type O to B3 in the vicinity of H II regions near $l = 328^\circ$. They identify an O6f star, LSS 3386, in the vicinity of RCW 94 at a distance of 2.3 kpc. They also identify an O7V star, BDMW123, at a distance of 3.3 kpc near RCW 95. While it is not clear whether these stars are *the* ionizing stars for these regions, their presence does seem to indicate a preference for the near distance of the distance ambiguity. We note, also, that at a distance of 3.1 kpc RCW 94 has a physical diameter of $\sim 17 \text{ pc}$, a typical diameter for an extended H II region. Whereas at a distance of 11.1 kpc, the physical diameter would be $\sim 62 \text{ pc}$, unusually large for an H II region. The diameter at the larger distance, as well as the nearby massive stars noted in Georgelin et al. (1994), are evidence favoring a distance of 3.1 kpc.

The H I emission morphology in the RCW 94-95 region between velocities of -35 km s^{-1} and -50 km s^{-1} is complicated. We have detected an H I shell surrounding RCW 94 centered at $v = -38 \text{ km s}^{-1}$. There is a ridge of H I centered at $l = 326^\circ.3$, $b = +0^\circ.8$ that lies just outside the continuum emission contours. This shell is shown in Fig. 10, where the greyscale is the H I channel image at $v = -38 \text{ km s}^{-1}$ and the contours are 21-cm continuum emission. The shell is apparent from $v = -35 \text{ km s}^{-1}$ to $v = -42 \text{ km s}^{-1}$. The shell itself is surrounded by a ring of decreased H I emission which, although not continuous, is also centered on the H II region. The emission shell has an average diameter of $\sim 24 \text{ pc}$, a thickness of $\sim 5 \text{ pc}$, and shows a brightness temperature increase from the interior to the shell edge of about a factor of two. The H I shell morphology closely matches the morphology of the H II regions, implying that the shell is indeed related to RCW 94.

The lack of H I inside to the shell is clearly due to ionization in the H II region. The origins of the shell are somewhat less clear. Using the column density integrated through the range of velocities including the shell we estimate that the H I mass of the shell is $\sim 170 M_\odot$. That the shell extends over $\sim 7 \text{ km s}^{-1}$ suggests that it may be expanding. The velocity gradient at this place in the Galaxy is $\sim 18 \text{ km s}^{-1} \text{ kpc}^{-1}$. Therefore a static shell with velocity width $\Delta v \approx 7 \text{ km s}^{-1}$ would have an extent of 380 pc along the line-of-sight. Since it is highly unlikely that the shell extends that far, we suggest that the velocity width is due to expansion such that $v_{exp} = \Delta v/2$. Assuming $v_{exp} \sim 4 \text{ km s}^{-1}$, we estimate the energy required to form this shell is on the order of $\sim 10^{51}$ ergs, which is consistent with the amount of energy expected from stellar

winds over the lifetime of a single massive star. Because of the low expansion velocity, the formation energy for a shell whose expansion has stalled is comparable.

We suggest that the H I shell and depression around RCW 94 are the signatures of a molecular cloud encircling the H II region. In this case, the H II region appears to be embedded in a molecular cloud, displaying various stages of ionization and dissociation related to the interior stars. Interior to the $\sim 24 \text{ pc}$ inner shell radius the UV photons from the stars ionize the neutral gas, producing the H II region. The stars photo-dissociate the surrounding molecular gas, producing an H I shell which extends to a radius of $\sim 29 \text{ pc}$. The H I morphology correspondence with the continuum morphology especially supports this hypothesis. In particular, the region of dense H I emission in the concave portion on the right-hand side of the H II region indicates that the expansion of the photo-dissociation region (PDR) was impeded by a density enhancement in the external medium, presumably clumps of molecular material. The extension of the shell surrounding the compact source to the upper left, indicates that the shape of the shell is directly related to the shape of the H II region, and that they are therefore correlated. Comparison with the CO images of Bronfman et al. (1989) indicates molecular gas at the position and velocity of RCW 94. Immediately exterior to the H I shell we can expect to see emission from polycyclic aromatic hydrocarbons (PAHs) at 6.2, 7.7, 8.6, or 11.3 μm (Simpson et al. 1999). Close examination of MSX band A data does reveal an increase in emission exterior to the H I shell, which also supports the theory that this H II region and its H I shell are embedded in a molecular cloud. Gaensler et al. (2000a) explore the polarization properties of this region and find that the depolarization is consistent with being caused by an H II region embedded in molecular gas with several layers of ionization and photo-dissociation.

The H I depression around RCW 94 appears to extend towards the Plane at lower longitudes where it traces the morphology of the large bow shaped structure, G326.96+0.03, seen at the bottom of the continuum image. This source is seen in the MOST images, as well as the MSX images, and therefore appears to be a thermal source. We measure H I absorption towards the knot of emission at $l = 326^\circ.95$, $b = +0^\circ.02$. Though the spectrum is rather noisy (Fig. 9 left), we see a strong absorption feature at $v = -60 \text{ km s}^{-1}$, which indicates that this region may be slightly more distant than RCW 94-95 ($d = 3.9 \text{ kpc}$), though still in the Scutum-Crux arm. There is an extended region of H I emission to the left of these H II regions which is much brighter than that surrounding RCW 94-95. The column density in this region, over the range of channels spanning the depression ($v = -38.4 \text{ km s}^{-1}$ to $v = -33.45 \text{ km s}^{-1}$), is a factor of two larger than it is surrounding the H I shell.

5.2. HI Shells

Whereas H II regions and SNRs draw a connection between the H I line and continuum emission, the impact of massive stars on the ISM can also be seen with H I shells, where no continuum object exists. These cavities survive much longer than the radiative lifetime of a SNR or an H II region, allowing us to explore the lasting effects of massive

stars on the ISM. H I shells are often detected as voids in the H I with brightened “walls” of swept-up material. These shells can range in size from tens of parsecs to kiloparsecs. The majority of the shells, especially the smaller ones, are caused by the combined effects of stellar winds and supernovae (Heiles 1984). The ultimate destruction of an H I shell occurs on the time-scale of tens of millions of years when they eventually dissipate as a result of turbulent motions in the ISM and shear due to differential rotation in the Galaxy.

We have detected two small shells in the SGPS Test Region (McClure-Griffiths et al. 2000a). The first of these appears as an H I void at $l = 329^\circ 3$, $b = +0^\circ 4$, $v = -108 \text{ km s}^{-1}$, the terminal velocity for this line of sight. The velocity implies a kinematic distance of 7.3 kpc. Fig. 11 is an H I channel image at $v = -108 \text{ km s}^{-1}$ showing a small shell of angular diameter is $\sim 0^\circ 4$. At a distance of 7.3 kpc the shell has a physical diameter of $\sim 50 \text{ pc}$. Because of its position at the terminal velocity it is very difficult to distinguish the front and back caps, we detect only the front cap. It is not unusual to detect only one cap, though. There is only one detectable cap for a large majority of the shells catalogued by Heiles (1984). Detecting only one cap makes it difficult to estimate an expansion velocity. It may be that the shell is stalled or that the structure is mostly cylindrical and expanding in the plane of the sky. Though we cannot measure the expansion velocity, we interpret this structure as a stalled wind or supernova blown shell.

The second shell is observed in the local gas at $v = -2.1 \text{ km s}^{-1}$, $l = 330^\circ 5$, and $b = +2^\circ 12$. This shell is shown in Fig. 12, a channel image of the H I at $v = -2.1 \text{ km s}^{-1}$. The shell is remarkably circular with an angular diameter of $\sim 2^\circ 5$. Because of its low velocity its distance is very uncertain, we estimate $D = 350 - 500 \text{ pc}$, which implies a physical radius of only $\sim 15 \text{ pc}$. Given its small size we speculate that this shell may have been formed by an old SNR. There are no associated features in the continuum image.

5.3. *Supernova Remnants*

5.3.1. *SNR G327.4+0.4*

H I studies of supernova remnants offer a great deal of information. H I absorption spectra allow us to place limits on the distances to SNRs, which lead to physical radii as well as age estimates. Examination of related H I emission structures may help us to understand why shell-type remnant morphology is dominated by loops and knots, in addition to diffuse emission. The morphology of SNRs is undoubtedly related in some complicated way to the inhomogeneities in the ISM into which they expand, as well as to non-uniform magnetic fields. One might expect SNR continuum emission to trace the local ISM in such a way that bright emission may be correlated with density enhancements exterior to the SNR shell. In principle these ISM density enhancements would be apparent as brightness temperature enhancements in the neutral hydrogen at velocities similar to the systemic velocity of the remnant. However, in practice it has proven difficult to correlate the continuum emission with emission structures in the H I (eg. Giacani et al. 2000).

We have extracted an absorption spectrum towards SNR

G327.4+0.4 as shown in Fig. 9, right side. The positive and negative wiggles in the range -85 to -95 km s^{-1} are a characteristic signature of variations in the terminal velocity, and cannot be trusted as real absorption. There is a strong absorption line centered at $v = -48 \text{ km s}^{-1}$, and a weaker, noisy line at about -70 km s^{-1} . There is no absorption corresponding to the emission peak at -80 km s^{-1} . We therefore adopt $V_L = -70 \text{ km s}^{-1}$ and $V_U = -80 \text{ km s}^{-1}$. These velocities indicate a distance of $4.3 \pm 0.5 \text{ kpc}$. This places the remnant on the far side of the Scutum-Crux Arm.

SNR G327.4+04 is a multi-arc shell-type SNR. The continuum emission has a bright, sharply bounded rim to the lower left, while the emission on the upper right side is much more diffuse. If the limb brightening observed to the lower left is a consequence of the shock impacting a density enhancement, we might expect to see an H I cloud exterior to the shell at the systemic velocity of the remnant. This is confirmed in the H I channel images at $v \approx -70 \text{ km s}^{-1}$, where we see a ridge of emission just exterior to the continuum contours. Fig. 13 is an average of two velocity channels centered at $v = -70 \text{ km s}^{-1}$ with continuum contours overlaid. There is an increase in H I density just exterior to the brightest portion of the SNR. In addition, the H I to the upper right, exterior to the less bright edge of the remnant, is much more diffuse. In this case it does appear that the continuum morphology is related to the surrounding H I.

SNR G327.4+0.4 has an angular diameter of $\sim 15' 3$, yielding a physical radius of $10.5 \pm 0.6 \text{ pc}$ at 4.3 kpc. To reinforce the point that this remnant must be at the near distance, we note that at 10.0 kpc the physical radius of the SNR would be an unusually large 22 pc. The radius allows us to estimate some fundamental parameters for the SNR. If the density of the medium into which the SNR expands is given by n_o (in cm^{-3}), the mass swept up by the SNR is $\sim 120n_o M_\odot$. As this mass is only a few times the presumed mass of the progenitor, we believe that the SNR is undergoing adiabatic expansion, but that it has only recently left the free expansion phase of evolution. Using the standard assumption that the SNR is in the Sedov-Taylor phase, we estimate the age $t_{\text{SNR}} = (5.3 \pm 0.8)(n_o/E_{51})^{1/2} \times 10^3 \text{ yr}$, where E_{51} is the input energy of the supernova explosion in units of 10^{51} ergs. If we assume typical values of $n_o = 0.2$ and $E_{51} = 1$ (Frail, Goss, & Whiteoak 1994), we find $t_{\text{SNR}} = (2.4 \pm 0.3) \times 10^3 \text{ yr}$.

5.3.2. *SNR G330.2+1.0*

We obtain an absorption spectrum towards SNR G330.2+1.0 which shows absorption out to $v = -80 \pm 6 \text{ km s}^{-1}$, indicating a minimum distance of $d = 4.9 \pm 0.3 \text{ kpc}$ for the supernova remnant. As noted in §3, this SNR has no clearly defined shell. There is continuum emission surrounding the brightened center. It is not clear how much of that emission is associated with the SNR. Fig. 14 is an H I image at $v = -80 \text{ km s}^{-1}$ overlaid with 21-cm continuum contours of SNR G330.2+1.0. At the low longitude end of G330.2+1.0 the lowest continuum contour extends in an arc away from the SNR center. Spatially offset from this edge the H I emission follows the same arc. Similarly, the continuum contour closest to the Plane

is bounded by H I emission which traces the contour. The morphological similarities between the lowest continuum contour and the H I emission to the right of the remnant suggests a possible correlation between the two. The overlap of H I from two distances at this velocity, as well as the small angular size of the SNR make it difficult to confirm whether the apparent H I-continuum correlation is real.

6. CONCLUSIONS

We have presented H I and $\lambda 21$ -cm data from the SGPS Test Region ($325^{\circ}5 \leq l \leq 333^{\circ}5$; $-0^{\circ}5 \leq b \leq 3^{\circ}5$), which are representative of the full Survey. These results highlight the interesting effects of massive stars on the ISM. The SGPS is ideal for studying the structure and dynamics of the H I in the inner Galaxy as it is sensitive to a large range of angular scales ($2' \lesssim \theta \lesssim 2^{\circ}$). In the Test Region we have explored the H I associated with three products of massive star life and death: H II regions, SNRs, and H I shells. Using H I absorption for systemic velocities and corresponding kinematic distances of H II regions and SNRs we are able to create a three dimensional picture of the distribution of the continuum sources in this region of the Galaxy.

We have highlighted several interesting H I and $\lambda 21$ -cm continuum emission features from the Test Region. The features in the continuum image include extended emission structures and a possible new SNR G328.6-0.0. Comparing the H I and continuum, we found an H I shell around the H II region RCW 94 which indicates that the H II region is embedded in a molecular cloud. In this case we see the reciprocal effects of massive stars and the surrounding H I during the stellar lifetime. The continuum emission morphology of the H II region closely matches the mor-

phology of the surrounding H I. We use H I absorption towards the SNRs G327.4+0.4 and G330.2+1.0 to determine kinematic distances of 4.3 and 4.9 kpc, respectively. H I at the systemic velocity of these remnants shows morphological similarities to the continuum emission. In particular, density enhancements were found exterior to regions of continuum limb-brightening for G327.4+0.4. We also found two small H I shells with no counterparts in continuum emission. We use the sizes and lack of detectable expansion velocity to interpret these structures as stalled supernova or wind blown shells which are older than the radiative lifetimes of either H II regions or SNRs.

Deciphering H I structure has always been challenging, but the recent availability of high resolution Galactic surveys such as the SGPS has improved the situation dramatically. Much of the inner Galaxy is completely filled with a variety of H I structures including shells, worms, sheets, and filaments. Though it is extremely difficult to determine the origins of many of the structures using H I emission data alone, combination with H I absorption and radio continuum emission measurements enables us to determine a three-dimensional, dynamical picture of the ISM.

We thank Veta Avedisova for supplying us with her extensive catalogue of star formation regions. This research has made use of the CDS SIMBAD database. JMD and NMM-G acknowledge support of NSF grant AST-9732695 to the University of Minnesota. NMM-G is supported by NASA Graduate Student Researchers Program (GSRP) Fellowship NGT 5-50250. BMG acknowledges the support of NASA through Hubble fellowship grant HST-HF-01107.01-A awarded by STScI, which is operated by AURA Inc. for NASA under contract NAS 5-26555.

REFERENCES

- Avedisova, V. S., 1997, *Baltic Astronomy*, 6, 307
- Bronfman, L., Alvarez, H., Cohen, R. S., & Thaddeus, P., 1989, *ApJS*, 71, 481
- Caswell, J. L. & Haynes, R. F., *A&A*, 171, 261
- Dickey, J. M., McClure-Griffiths, N. M., Gaensler, B. M., Green, A. J., Haynes, R. F., Wieringa, M. H., 2000, in preparation
- Dickey, J. M., McClure-Griffiths, N., Gaensler, B., Green, A., Haynes, R., Wieringa, M., 1999, in *New Perspectives on the Interstellar Medium*, ASP Conf. Ser. 168, eds. A. R. Taylor, T. L. Landecker & G. Joncas, (San Francisco: ASP), 27
- Dickey, J. M., 1997, *ApJ*, 488, 258
- Dickey, J. M., Brinks, E., & Puche, D., 1992, *ApJ*, 385, 501
- Egan, M. P., Shipman, R. F., Price, S. D., Carey, S. J., Clark, F. O., & Cohen, M. 1998, *ApJ*, 494, L199
- Fich, M., Blitz, L., & Stark, A. A., 1989, *ApJ*, 342, 272
- Frail, D. A., Goss, W. M., Whiteoak, J. B. Z., 1994, *ApJ*, 437, 781
- Frail, D. A. & Weisberg, J. M., 1990, *AJ*, 100, 743
- Frater, R. H., Brooks, J. W., & Whiteoak, J. B., 1992, *J. Electr. Electron. Eng. Aust.*, 12, 103
- Gaensler, B. M., Dickey, J. M., McClure-Griffiths, N. M., Green, A. J., Wieringa, M. H., Haynes, R. F., 2000a, *ApJ*, 549, in press
- Gaensler, B. M., Dickel, J., Green, A. J., 2000b, *ApJ*, 542, 380
- Georgelin, Y. M. & Georgelin, Y. P., 1976, *A&A*, 49, 57
- Georgelin, Y. M., Amram, P., Georgelin, Y. P., le Coarer, E., & Marcelin, M., 1994, *A&AS*, 108, 513
- Giacani, E. B., Dubner, G. M., Green, A. J., Goss, W. M. & Gaensler, B. M. 2000, *AJ*, 119, 281
- Gooch, R. E., 1996, in *Astronomical Data Analysis Software and Systems V*, ASP Conf. Ser. 101, ed. G. H. Jacoby & J. Barnes, (San Francisco: ASP), 80
- Goss, W. M. & Shaver, P. A., 1970, *AuJPA*, 14, 1
- Green, A. J., Cram, L. E., Large, M. I., & Ye, T., 1999, *ApJS*, 122, 207
- Green, D. A., 2000, *A Catalogue of Galactic Supernova Remnants* (2000 August version), (Cambridge: Mullard Radio Astronomy Observatory, Cavendish Laboratory) (<http://www.mrao.cam.ac.uk/surveys/snrs/>)
- Haynes, R. F., Staveley-Smith, L., Mebold, U., Kalberla, P., White, G., Jones, P., Dickey, J., Green, A., 1998, in *New Views of the Magellanic Clouds*, IAU Symp. 190, eds. Y.-H. Chu, N. Suntzeff, J. Hesser, & D. Bohlender, (San Francisco: ASP), 108
- Heiles, C., 1984, *ApJS*, 55, 585
- Kalberla, P. M. W., Mebold, U., and Reich, W., 1980, *A&A*, 82, 275
- Kuchar, T. A. & Bania, T. M., 1994, *ApJ*, 436, 117
- McClure-Griffiths, N. M., Dickey, J. M., Gaensler, B. M., Green, A. J., Haynes, R. F., Wieringa, M. H., 2000a, *PASA*, accepted
- McClure-Griffiths, N. M., Dickey, J. M., Gaensler, B. M., Green, A. J., Haynes, R. F., Wieringa, M. H., 2000b, *AJ*, 119, 2828
- McClure-Griffiths, N. M., Dickey, J. M., Gaensler, B. M., Green, A. J., Haynes, R. F., Wieringa, M. H., 1999, *BAAS*, 194, 0402
- Rodgers, A. W., Campbell, C. T., Whiteoak, J. B., 1960, *MNRAS*, 121, 103
- Reynolds, J. E., 1994, *ATNF Technical Document Series*, (Sydney: Australia Telescope National Facility), AT/39.3/0400 (http://www.narrabri.atnf.csiro.au/observing/users_guide/html/node215.htm)
- Sault, R. J., Staveley-Smith, L. & Brouw, W. N., 1996, *A&AS*, 120, 375
- Sault, R. J., Killeen, N. E. B., 1998, *The Miriad User's Guide*, (Sydney: Australia Telescope National Facility) (<http://www.atnf.csiro.au/computing/software/miriad/>)
- Shaver, P. A., McGee, R. X., & Pottasch, S. R., 1979, *Nature*, 280, 476
- Simpson, J. P., Witteborn, F. C., Cohen, M., Price, S. D., 1999, in *The Central Parsecs of the Galaxy*, ASP Conf. Ser. 186, eds. H. Falcke, A. Cotera, W. J. Duschl, F. Melia, & M. J. Rieke, (San Francisco: ASP), 527
- Stanimirović, S., 1999, PhD Thesis, University of Western Sydney, Nepean

- Stanimirović, S., Staveley-Smith, L., Dickey, J. M., Sault, R. J., & Snowden, S. L., 1998, MNRAS, 301, 417
- Staveley-Smith, L., Wilson, W. E., Bird, T. S., Disney, M. J., Ekers, R. D., Freeman, K. C., Haynes, R. F., Sinclair, M. W., Vaile, R. A., Webster, R. L., Wright, A. E., 1996, PASA, 13, 243
- Taylor, A. R., 1999, in *New Perspectives on the Interstellar Medium*, ASP Conf. Ser. 168, eds. A. R. Taylor, T. L. Landecker & G. Joncas, (San Francisco: ASP), 3
- Taylor, J. H. & Cordes, J. M., 1993, ApJ, 411, 674
- Weaver, H. F. & Williams, D. R. W., 1974, A&AS, 17, 251
- Whiteoak, J. B. Z. & Green, A. J., 1996, A&AS, 118, 329
- Whiteoak, J. B. Z., Cram, L. E., & Large, M. I., 1994, MNRAS, 269, 294
- Williams, D., 1973, A&AS, 8, 505

FIG. 1.— 21-cm continuum image of the SGPS Test Region from the ATCA with the 190 pointing centers marked. The greyscale is linear and runs from $-0.03 \text{ mJy beam}^{-1}$ to $0.1 \text{ mJy beam}^{-1}$ as shown in the wedge at the right. The image has an rms noise of $5.5 \text{ mJy beam}^{-1}$. The beam is $124''.9 \times 107''.5$ and is displayed in the upper left of the image.

FIG. 2.— Channel images from the combined Parkes and ATCA continuum subtracted H I line cube of the Test Region. Every fourth channel is displayed for a velocity separation of 3.2 km s^{-1} . The greyscale is linear from 0 K to 115 K and shown in the wedge at the right. The beam size is $124''.9 \times 107''.5$ and the rms noise is $\sim 2.3 \text{ K}$.

FIG. 2.— Continued

FIG. 2.— Continued

FIG. 2.— Continued

FIG. 3.— Continuum image of the 21-cm emission in the SGPS Test Region. The image includes both ATCA and Parkes data. The greyscale is linear and runs from 0.5 to 1.1 Jy beam^{-1} as shown in wedge at the right. The rms noise is $\sim 7 \text{ mJy beam}^{-1}$. The beam is shown in the upper left corner and is $124''.9 \times 107''.5$.

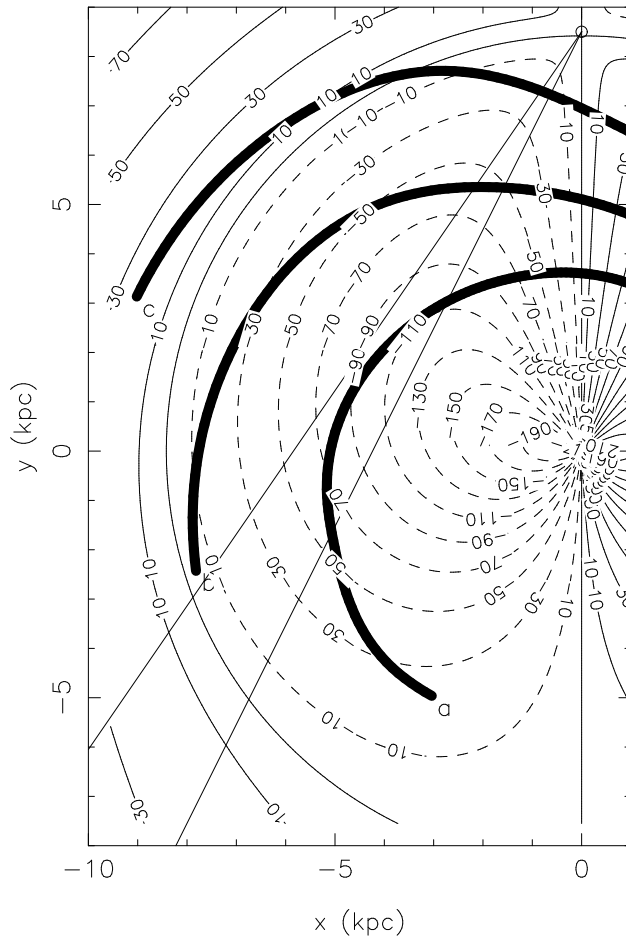


FIG. 4.— Theoretical isovelocity contours calculated from the rotation curve of Fich, Blitz, & Stark (1989) and overlaid on the spiral pattern of the Galaxy from Taylor & Cordes (1993). The coordinates x and y are with respect to the Galactic center. The heavy black lines mark the approximate positions of the spiral arms. The spiral arms are labeled as **a**: Norma; **b**: Scutum-Crux; and **c**: Sagittarius-Carina. Contours are labeled with their LSR velocities, where dashed contours denote negative velocities and solid contours denote positive velocities. The two thin lines forming a wedge mark the SGPS Test Region line of sight. The line of sight covers the theoretical velocity range $-120 \text{ km s}^{-1} \leq v \leq 80 \text{ km s}^{-1}$. The approximate positions of the spiral arms in velocity space can be discerned from the velocity contours that they cross.

FIG. 5.— 843 MHz continuum image of the SGPS Test Region from the MOST Galactic Plane Survey (Green et al. 1999). Prominent H II regions and SNRs are labeled. The greyscale is linear and runs from $-30 \text{ mJy beam}^{-1}$ to 60 mJy beam^{-1} , as shown in the wedge at the left. The beamsize for the MOST survey is $43''.0 \times 51''.9$ and the rms noise is $\sim 2.2 \text{ mJy beam}^{-1}$.

FIG. 6.— Images of a possible new SNR G328.6-0.0. To the left, image a, is 843 MHz continuum emission from the MOST Galactic Plane Survey (Green et al. 1999). The image at the right, image b, is 1420 MHz continuum emission from the SGPS. The rms noise of the MOST image is ~ 2.2 mJy beam $^{-1}$ and the beamsize is $43''.0 \times 51''.9$. The rms noise of the SGPS image is ~ 7 mJy beam $^{-1}$ and the beamsize is $124''.9 \times 107''.5$. The possible SNR is the large loop in the center of the image.

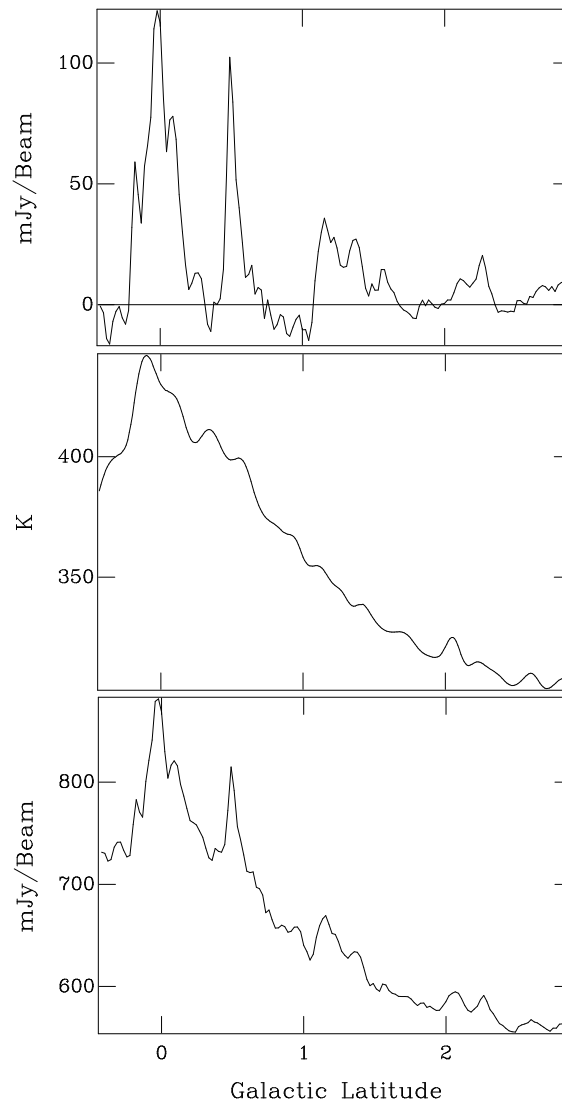


FIG. 7.— Slices across the SGPS Test Region continuum image at $l = 328.7$ using only the ATCA data (top), only the Parkes data (center), and the combined Parkes and ATCA data (bottom). Individual sources are resolved in the ATCA slice, whereas the Parkes data detects the Galactic background. The combined data show individual sources superimposed on the Galactic background.

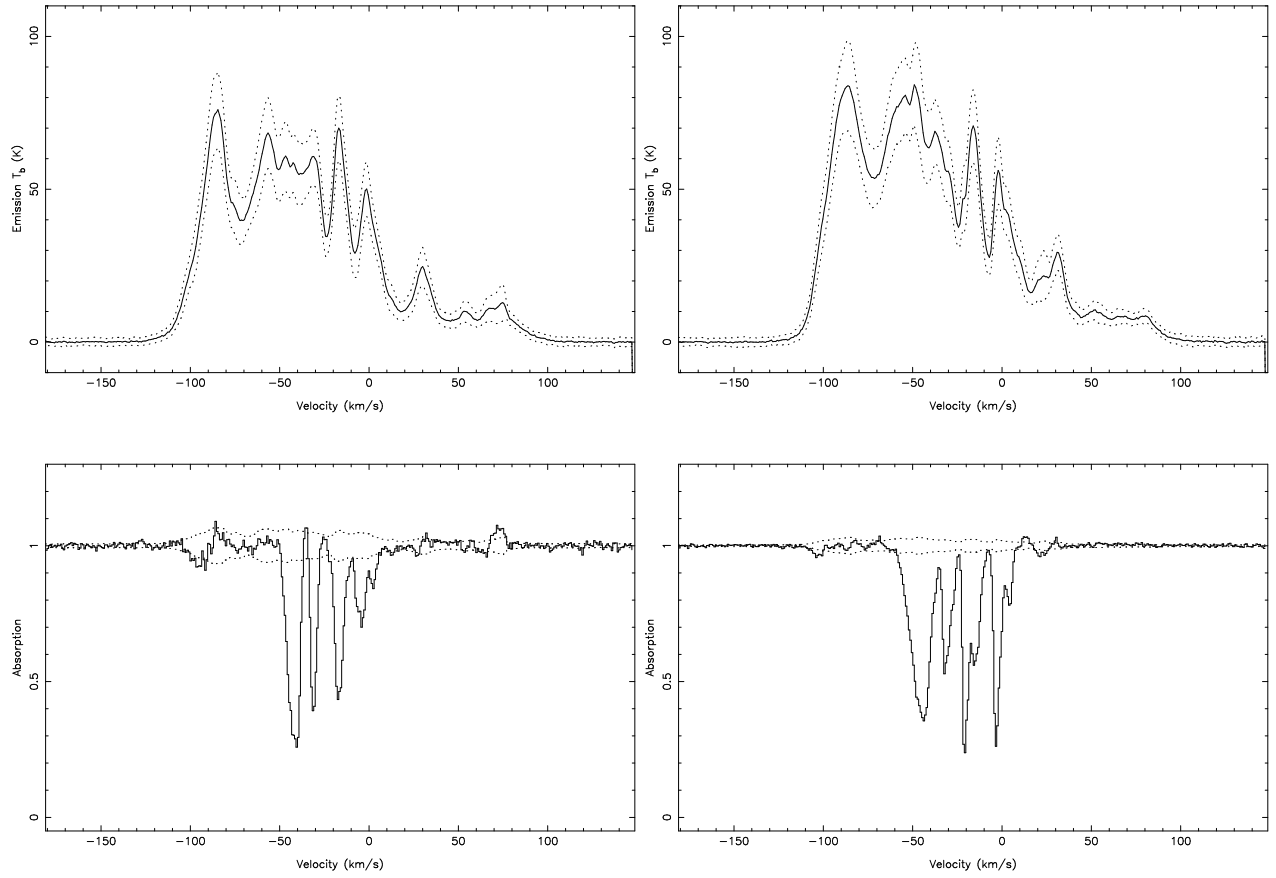


FIG. 8.— H I emission (top) and absorption (bottom) spectra taken towards RCW 94 (left) and G326.65+0.59 (right). The top panels are interpolated emission around the source. The dashed lines mark the calculated 1σ error envelope of the interpolated emission. The bottom panels plot $e^{-\tau}$ and associated 1σ errors towards the H II regions.

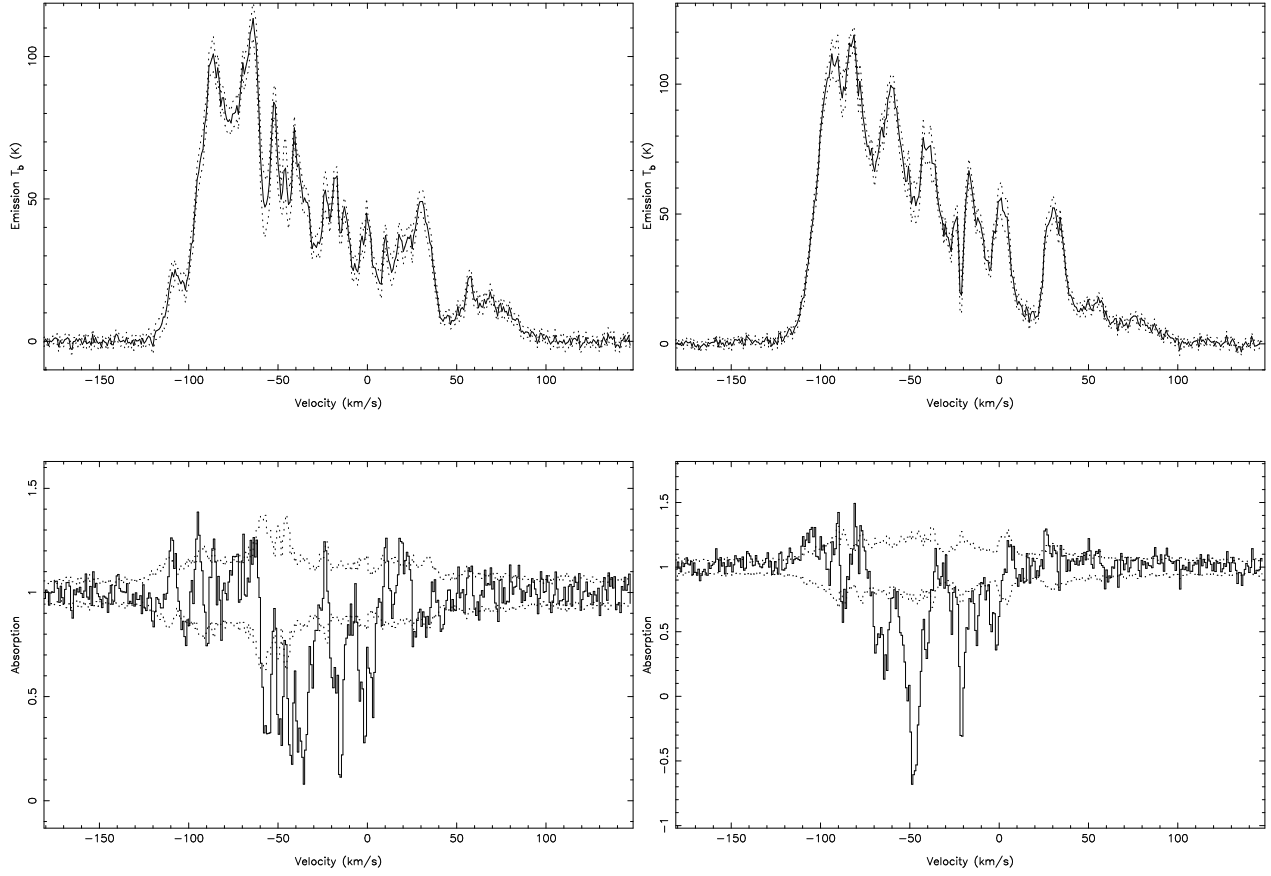


FIG. 9.— H I emission and absorption towards G326.96+0.03 (left) and towards SNR G327.4+0.4 (right). The panels are the same as Fig. 8.

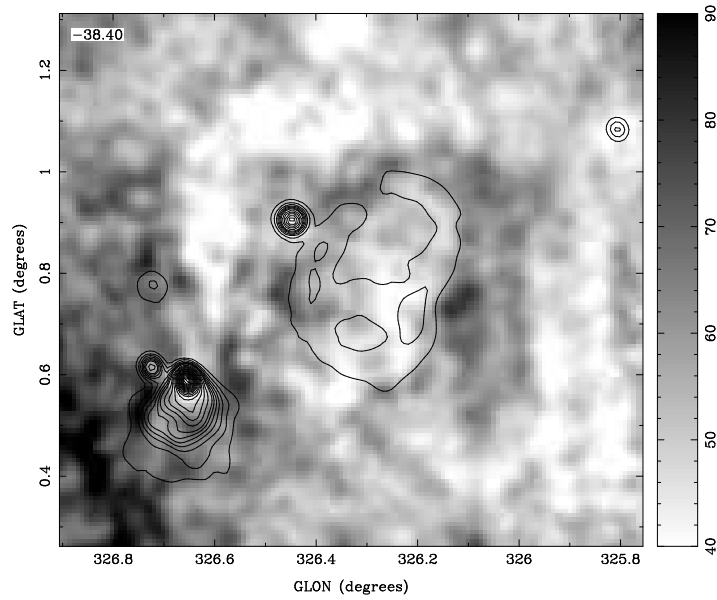


FIG. 10.— Greyscale H I channel image at $v = -38 \text{ km s}^{-1}$ of the region surrounding the RCW 94-95 H II complex; 21-cm continuum contours are overlaid. The greyscale is linear and runs from 40 to 90 K as shown in the wedge on the right. The continuum contours are at 0.2 Jy beam $^{-1}$ intervals from 0.6 Jy beam $^{-1}$ to 10 Jy beam $^{-1}$. The beam size is $124''.9 \times 107''.5$ and the rms noise is $\sim 2.3 \text{ K}$ in the line and $\sim 7 \text{ mJy beam}^{-1}$ in the continuum. The small H I shell, centered at $l = 326^\circ 3$, $b = +0^\circ 8$ is identified by the ring of H I emission around the H II region contours.

FIG. 11.— Greyscale image of an H I channel image at $v = -108 \text{ km s}^{-1}$ showing an apparent H I shell in the ISM at the terminal velocity. The greyscale is linear from 0 K to 80 K, as shown in the wedge on the right. The beam size is $124''.9 \times 107''.5$ and the rms noise is $\sim 2.3 \text{ K}$. The small shell, of diameter $\sim 0''.4$, is located at $l = 329^\circ.3$, $b = +0^\circ.4$ and is identified by the bright ring of emission surrounding the H I void.

FIG. 12.— Greyscale H I channel image at $v = -2.12 \text{ km s}^{-1}$ showing an apparent H I shell in the local ISM at $l = 330^\circ.5$, $b = +2^\circ.2$. The greyscale is logarithmic to emphasize the shell walls. The brightness temperature scale in Kelvins (35 K to 90 K) is displayed in the wedge on the right. The beam size is $124''.9 \times 107''.5$ and the rms noise is $\sim 2.3 \text{ K}$.

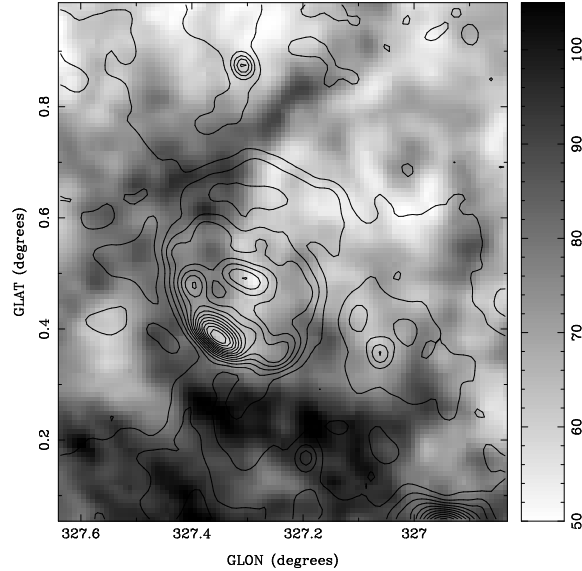


FIG. 13.— SNR G327.7+0.4. Greyscale image of an average of two H I velocity channels centered at $v = -70 \text{ km s}^{-1}$. The greyscale is linear and runs from 50 to 105 K, as shown in the wedge at the right. The contours show the 21-cm continuum emission from SNR G327.7+0.4 at intervals of 60 mJy beam^{-1} from $300 \text{ mJy beam}^{-1}$ to 2 Jy beam^{-1} . The beam size is $124''.9 \times 107''.5$ and the rms noise is $\sim 2.3 \text{ K}$ in the line and $\sim 7 \text{ mJy beam}^{-1}$ in the continuum.

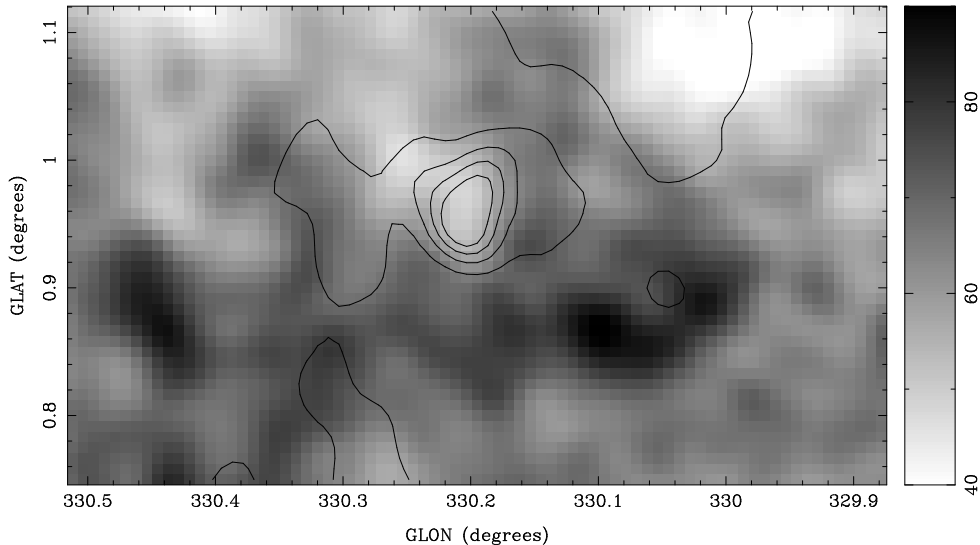


FIG. 14.— SNR G330.2+1.0. Greyscale image of an average of two H I velocity channels centered at $v = -80 \text{ km s}^{-1}$. The greyscale is linear and runs from 40 to 90 K, as shown in the wedge at the right. The contours show the 21-cm continuum emission from SNR G330.2+1.0 from $210 \text{ mJy beam}^{-1}$ to 2.1 Jy beam^{-1} at intervals of $105 \text{ mJy beam}^{-1}$. The beam size is $124''.9 \times 107''.5$ and the rms noise in the line is $\sim 2.3 \text{ K}$ and $\sim 7 \text{ mJy beam}^{-1}$ in the continuum. The H I emission roughly traces the outermost continuum contour.

TABLE 1

TABLE OF OBSERVING DATES AND TELESCOPE OR ARRAY CONFIGURATIONS FOR THE TEST REGION.

Date	Array	UT
1997 Apr 21	0.375	09:22 - 22:14
1997 Apr 22	0.375	08:00 - 22:05
1997 Apr 23	0.375	12:11 - 22:03
1997 Aug 11	0.75B	05:33 - 16:06
1997 Aug 13	0.75B	08:33 - 15:51
1997 Oct 25	0.75C	20:53 - 11:12
1998 Mar 30	0.375	10:00 - 20:40
1998 Apr 20	0.75A	08:06 - 20:59
1998 Apr 21	0.75A	07:44 - 21:02
1998 Dec 14-15	Parkes	20:16 - 05:21
1998 Dec 15-16	Parkes	20:22 - 06:33
1998 Dec 16	Parkes	14:56 - 22:30

TABLE 2
TABLE OF H I ABSORPTION VELOCITIES AND KINEMATIC DISTANCES FOR EXTENDED CONTINUUM SOURCES.

Source	l (deg)	b (deg)	H I V_L^a (km s ⁻¹)	H I V_U (km s ⁻¹)	H109 α & H110 α^b V (km s ⁻¹)	D_L^c (kpc)	D_U^c (kpc)	R_{gal}^d (kpc)
RCW 94	326.45	+0.91	-42	-48	-45	2.9	3.3	6.2
G326.65+0.59	326.66	+0.59	-47	-60	-44	3.2	3.9	6.0
G326.96+0.03	326.95	+0.02	-57	-62	-64	3.7	4.0	5.6
SNR G327.4+0.4 (Kes 27)	327.34	+0.40	-67	-82	...	4.3	5.4	5.2
G327.99-0.09	327.99	-0.09	-52	-68	-45	3.5	4.3	5.7
G328.31+0.45	328.30	+0.44	-96	-101	-97	6.0	6.5	4.6
SNR G328.4+0.2 (MSH 15-57)	328.42	+0.22	+28	17.4	...	11.1
G329.35+0.14	329.34	+0.14	-103	-109	-107	6.4	7.3	4.4
G329.49+0.21	329.47	+0.21	-100	-109	-102	6.1	7.3	4.5
SNR G330.2+1.0	330.21	+0.97	-80	4.9(9.9) ^e	...	4.9
G331.03-0.15	331.05	-0.16	-95	-100	-89	5.5	5.9	4.5
G331.26-0.19	331.27	-0.19	-89	-100	-85	5.3	5.9	4.5
G331.52-0.07	331.52	-0.08	-92	-102	-89	5.5	6.0	4.4

^aAll velocities all quoted with respect to the local standard of rest (LSR).

^bFrom Caswell & Haynes (1987).

^cDistances are derived using a standard rotation curve as in Fich, Blitz & Stark (1989), assuming IAU standard parameters of $\Theta_o = 220$ km s⁻¹ and $R_o = 8.5$ kpc.

^d R_{gal} values are calculated at the lower velocity limit.

^eValues in parentheses are the more distant for velocities interior to the solar circle.

This figure "figure1.jpg" is available in "jpg" format from:

<http://arxiv.org/ps/astro-ph/0012302v1>

This figure "figure2a.jpg" is available in "jpg" format from:

<http://arxiv.org/ps/astro-ph/0012302v1>

This figure "figure2b.jpg" is available in "jpg" format from:

<http://arxiv.org/ps/astro-ph/0012302v1>

This figure "figure2c.jpg" is available in "jpg" format from:

<http://arxiv.org/ps/astro-ph/0012302v1>

This figure "figure2d.jpg" is available in "jpg" format from:

<http://arxiv.org/ps/astro-ph/0012302v1>

This figure "figure3.jpg" is available in "jpg" format from:

<http://arxiv.org/ps/astro-ph/0012302v1>

This figure "figure5.jpg" is available in "jpg" format from:

<http://arxiv.org/ps/astro-ph/0012302v1>

This figure "figure6.jpg" is available in "jpg" format from:

<http://arxiv.org/ps/astro-ph/0012302v1>

This figure "figure11.jpg" is available in "jpg" format from:

<http://arxiv.org/ps/astro-ph/0012302v1>

This figure "figure12.jpg" is available in "jpg" format from:

<http://arxiv.org/ps/astro-ph/0012302v1>